METALLURGY

Segregation-induced ordered superstructures at general grain boundaries in a nickel-bismuth alloy

Zhiyang Yu,[1]* Patrick R. Cantwell,[2] Qin Gao,[3] Denise Yin,[1] Yuanyao Zhang,[4] Naixie Zhou,[4] Gregory S. Rohrer,[5] Michael Widom,[3] Jian Luo,[4]† Martin P. Harmer[1]†

The properties of materials change, sometimes catastrophically, as alloying elements and impurities accumulate preferentially at grain boundaries. Studies of bicrystals show that regular atomic patterns often arise as a result of this solute segregation at high-symmetry boundaries, but it is not known whether superstructures exist at general grain boundaries in polycrystals. In bismuth-doped polycrystalline nickel, we found that ordered, segregation-induced grain boundary superstructures occur at randomly selected general grain boundaries, and that these reconstructions are driven by the orientation of the terminating grain surfaces rather than by lattice matching between grains. This discovery shows that adsorbate-induced superstructures are not limited to special grain boundaries but may exist at a variety of general grain boundaries, and hence they can affect the performance of polycrystalline engineering alloys.

Many properties of polycrystalline metals and ceramics are intimately linked to the structure and composition of their grain boundaries (*1*). Alloying elements, dopants, and impurities are often present in higher concentrations at grain boundaries than in grain interiors, an effect known as grain boundary segregation or adsorption. Segregation can enhance macroscopic properties (*2*) but often leads to severe degradation of properties and performance (*3*, *4*). Understanding how and why this degradation occurs at the atomic scale is a crucial step toward engineering innovative materials that can resist such deleterious effects.

A recent advance in materials engineering is the discovery that grain boundaries behave in a phase-like manner, transitioning from one state to another as a function of temperature and composition (*5*–*8*). The term "complexion" has been introduced to distinguish such interfacial states from bulk phases (*9*). Complexions have been discovered at dislocations (*10*), twin boundaries (*11*), and stacking faults (*12*), and they play a role in nanocrystalline alloys (*13*). However, the exact structural arrangement of adsorbates within complexions and the resultant impact on properties are still largely unknown.

[1]Department of Materials Science and Engineering, Lehigh University, Bethlehem, PA 18015, USA. [2]Department of Mechanical Engineering, Rose-Hulman Institute of Technology, Terre Haute, IN 47803, USA. [3]Department of Physics, Carnegie Mellon University, Pittsburgh, PA 15213, USA. [4]Department of NanoEngineering, Program of Materials Science and Engineering, University of California, San Diego, La Jolla, CA 92093, USA. [5]Department of Materials Science and Engineering, Carnegie Mellon University, Pittsburgh, PA 15213, USA.
*Present address: School of Materials Science and Engineering, Xiamen University of Technology, Xiamen 361024, China.
†Corresponding author. Email: mph2@lehigh.edu (M.P.H.); jluo@alum.mit.edu (J.L.)

The atomic structure and solute segregation of grain boundaries are often analyzed by transmission electron microscopy (TEM) in ceramics (*2*, *14*–*18*) and metals (*4*, *19*–*21*); more recently, atom probe tomography (APT) has become a useful tool for grain boundaries because of its complementary analytical strengths (*22*–*24*). However, only a handful of studies have examined the structural arrangement of adsorbates at general grain boundaries in polycrystalline materials [e.g., (*15*–*18*, *20*, *21*)]. Some degree of grain boundary adsorbate periodicity was evident in a few of these studies, such as along one side of nanometer-thick intergranular "glassy" films in Si_3N_4 (*16*–*18*), but no evidence of widespread adsorbate-induced grain boundary superstructures has been reported. In contrast to these studies, TEM studies on special high-symmetry boundaries, such as tilt (*2*, *4*, *14*, *19*) and twist (*25*) boundaries in artificial bicrystals, often reveal striking, periodic patterns of segregated elements—for example, in Bi-doped Cu (*4*) and rare earth–doped alumina (*2*). We also note that an interface reconstruction has been observed at a Ni-Al_2O_3 phase boundary (*26*).

Unlike the grain boundaries in high-symmetry tilt or twist bicrystals, the majority of grain boundaries in polycrystalline materials are of mixed twist and tilt character. Mixed boundaries are sometimes called "random" or "general" grain boundaries (*27*). The common definition of a general grain boundary is one with a large inverse coincidence ($\Sigma > 29$) (*8*). Although this Σ-based definition has received criticism (*28*), it is widely used (*29*), so for the purposes of the present work, a general boundary is simply one that lacks appreciable lattice coincidence. General grain boundaries are populous in polycrystalline engineering materials and are often weaker mechanically and chemically than higher-symmetry special grain boundaries, and thereby can limit macroscopic properties and performance. Hence, understanding these performance-limiting grain boundaries is critical to enhancing our ability to engineer next-generation materials (*8*, *30*).

Our previous work on liquid-metal embrittlement of Ni by Bi showed two Bi-rich layers visible at the grain boundary with linear periodicity (*21*). However, it was unclear whether the segregated adsorbate atoms had superstructures. Here, we present experimental results from scanning TEM (STEM) and simulated results from density functional theory (DFT) to demonstrate that a variety of periodic adsorbate superstructures form at naturally occurring, randomly selected general grain boundaries in Bi-infused polycrystalline nickel. We discovered that the grain boundary reconstructions at these boundaries are not driven by the grain boundary misorientation, as commonly believed, but by the crystallographic orientation of the grain boundary plane. In this way, these grain boundary reconstructions are strongly analogous to surface reconstructions, which are also driven by the crystallography of the terminating surface and which alter the two-dimensional translational symmetry of the interface, influencing surface diffusion coefficients (*31*), electronic characteristics (*32*), and other physical properties.

We randomly selected 12 grain boundaries from a Bi-infused Ni polycrystalline specimen and examined them by aberration-corrected STEM (table S1 and figs. S1 to S14) (*33*). The Ni-Bi alloy has the equilibrium solidus composition at 700°C, which we estimated to be 0.22 atomic percent Bi in Ni based on recent CALPHAD data (*34*). The misorientation of all 12 randomly selected grain boundaries was determined via a detailed Kikuchi diffraction pattern analysis. Calculations (*35*) done with these misorientation data showed that 11 of the 12 boundaries were general grain boundaries with Σ values greater than 500 (table S1). One of the 12 boundaries was determined to be a Σ3 twin boundary. Bi adsorbate superstructures were discovered at many of the general grain boundaries, and the Bi segregation was confirmed by energy-dispersive x-ray spectroscopy (fig. S15).

We use two different categories of notation to describe the Bi adsorbate superstructures: (i) When discussing the arrangement of Bi atoms within the grain boundary plane, we use Wood's notation (*36*) [e.g., Fig. 1 shows a C(2×2) reconstruction] or matrix notation (*37*) (e.g., Figure 2 includes results for the [5–511] reconstruction, which cannot be clearly represented by Wood's notation), both common in surface science. (ii) When discussing how the Bi adsorbate atoms appear when viewed from the side in projection (i.e., as in TEM images), we refer to the number of Bi atoms that appear to be sitting on top of a given number of Ni atoms (e.g., Fig. 1B shows a 2Bi/4Ni superstructure, the side view of Fig. 1A parallel to [010]).

We observed the simplest Bi adsorbate pattern of 2Bi/4Ni for the (100) grain boundary facet (Fig. 1, A to D). The (110) grain boundary facet (Fig. 1, E to H) exhibits a 3Bi/6Ni superstructure when viewed from the side parallel to $[1\bar{1}1]$. Both of these superstructures reduce to an apparent 1Bi/2Ni superstructure when viewed from the

side, if the primitive repeat unit is considered. Finally, the (111) grain boundary facet (Fig. 1, I to L) exhibits a 10Bi/16Ni superstructure when viewed parallel to [1$\bar{1}$0], which reduces to a 5Bi/8Ni primitive repeat unit. Additionally, we observed a 5Bi/10Ni superstructure (fig. S22) on the (111) boundary plane.

The TEM images in Fig. 1 are two-dimensional projections and do not provide the three-dimensional atomic arrangements in the plane of the grain boundary. To address this issue, we conducted DFT calculations of relaxed-surface free energies for various low-energy superstructures for the corresponding low-index crystallographic planes (Fig. 2). The atomic models from the DFT calculations form Bi superstructures nearly identical to the experiments when viewed from the side (Fig. 1). We note that although DFT surface calculations in general may not capture the key features of grain boundaries in other alloys, our previous work (*38*) has shown that surface DFT calculations are a reasonable approximation for grain boundaries in Ni-Bi alloys because (i) the total energy of Ni-Bi grain boundaries can be predicted with tolerable accuracy from the energies of the two surfaces alone, and (ii) the Bi-Bi atomic bonds across the Bi-rich bilayer at the grain boundary are weak relative to Bi-Ni bonds on either side of the boundary. This latter point is demonstrated by the bonding charge distributions illustrated in Fig. 2, as discussed below.

The grain boundaries we analyzed in the experimental images were taken from Bi-saturated Ni specimens in equilibrium with the Bi-rich liquid, as we prepared them under liquid-metal embrittlement conditions, although some local variations in Bi chemical potential likely exist because of kinetic factors (*33*). In the case of the (100) and (111) grain boundary facets in Fig. 1, the DFT-calculated surface superstructures (Fig. 1, A and I, and figs. S26 and S28) correspond to a superstructure that exists in a low-energy state for at least one chemical potential (Fig. 2, A and C). For the (100) surface, one low-energy superstructure is the C(2×2) surface reconstruction (fig. S20), as shown in Fig. 1A. For the (111) surface, the (8×8) reconstruction (fig. S23) is one of the stable reconstructions based on the DFT surface calculations, as shown in Fig. 1I. In addition, the [5–511] structure (fig. S22) on a Ni(111) surface has comparable energy to the (8×8) reconstruction (Fig. 2C) and is also considered as a stable structure. For the (110) surface (Fig. 1E), DFT calculations show that three different reconstructions (figs. S21 and S27) have similar energy at a chemical potential near the bare Ni surface: (2×2), C(2×2), and a randomly centered superlattice of C(2×2) that we term (2×2)-RandC. This similarity suggests a superstructure for the (110) surface in which the basic motif is (2×2) with random centering (in Fig. 1E, atoms that are half white and half magenta represent Bi sites that are randomly occupied). This random occupation of the centering atoms is consistent with Fig. 1, G and H, where variable-intensity Bi columns contrast with the strong intensity of the other columns. Taken together, we suggest that superstructures in Bi-doped Ni grain boundaries closely resemble surface reconstructions.

The surface free energy varies as a function of chemical potential for a series of different Bi-based superstructures based on our DFT calculations (Fig. 2, A to C). Charge density figures (Fig. 2, D to F) depict the bonding between Ni and Bi atoms for three model superstructures, two at surfaces and one at a grain boundary, in which red indicates increased charge density and green indicates a depletion of charge. Our figures illustrate relaxed surface and grain boundary geometries together with the bonding charge density $\Delta\rho(r)$, defined as

$$\Delta\rho(r) = \rho^{SC}_{Tot}(r) - \rho^{SC}_{Ni}(r) - \rho^{atomic}_{Bi}(r) \quad (1)$$

where ρ^{SC} indicates a self-consistent interacting charge density, ρ^{atomic} indicates a superposition of isolated atomic charge densities, and the subscripts Tot, Ni, and Bi respectively refer to the complete Bi-on-Ni structure, the Ni atoms alone, and the Bi atoms alone. Hence, $\Delta\rho$ highlights the charge transfer due to Bi-Ni and Bi-Bi chemical bonding.

Positive ρ^{SC} between atoms (red in Fig. 2, D to F) indicates formation of chemical bonds occupied by electrons drawn away from the atoms, resulting in negative ρ^{SC} (green in Fig. 2, D to F) surrounding the atoms. Figure 2D shows that on an unreconstructed 1×1 Bi monolayer, the Bi atoms bond to each other but do not bond to the Ni surface. In the C(2×2) structure (Fig. 2E), the atoms bond to the Ni surface but not to each other. The grain boundary charge density figure in Fig. 2F shows the bonding of Bi to the adjacent Ni surfaces, whereas the lack of charge density across the boundary suggests a marked loss of cohesion (*38*, *39*). This result is consistent with the effect of liquid-metal embrittlement in this system, which is to drastically reduce the cohesive strength across the grain boundaries.

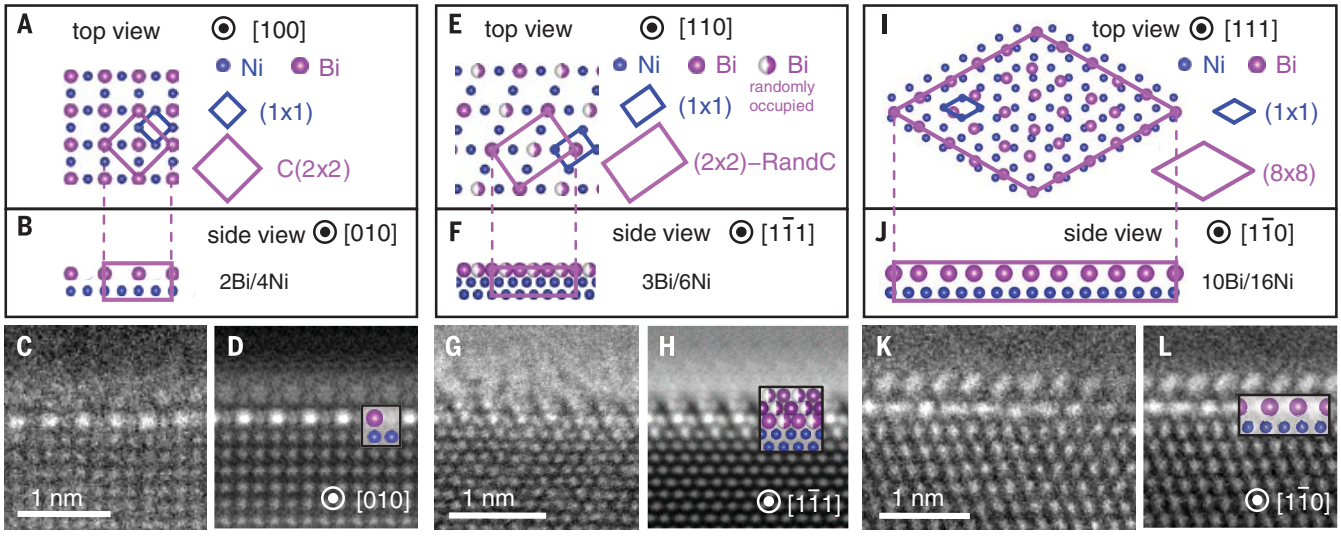

Fig. 1. Atomic-scale segregation–induced superstructures in the Ni-Bi system. (**A** to **D**) (100) crystallographic facets; (**E** to **H**) (110) crystallographic facets; (**I** to **L**) (111) crystallographic facets. These facets belong to grain boundaries #7, #2, and #5, respectively (table S1). HAADF-STEM images of Bi-based grain boundary superstructures [original images, (C), (G), and (K); averaged images, (D), (H), and (L)] show periodic arrangements of Bi atoms that are crystallographically related to the underlying nickel grains. Surface DFT calculations produce Bi-based superstructures [(A), (E), and (I)] that exhibit the same periodicity as the Bi adsorbate atoms in the HAADF-STEM images [(C), (D), (G), (H), (K), and (L)] when viewed from the side as two-dimensional projections [(B), (F), and (J)]. The HAADF-STEM images in (D), (H), and (L) have been averaged following the algorithm in (*51*) to help to determine the exact location of the Bi atoms. Note that the 3Bi/6Ni two-dimensional superstructure in (F) appears as 3Bi/6Ni when viewed in this direction if the lower-intensity, randomly centered Bi atoms are not counted.

General grain boundaries in Bi-infused Ni exhibit a morphology that comprises alternating facets (Fig. 3A). Atomic-resolution images of these facets (Fig. 3, B to E) reveal Bi-based superstructures similar to the superstructures in Fig. 1. Two crystal planes, one from each grain, join at each facet to produce the grain boundary. We determined the crystallographic indices of the four marked boundary planes in Fig. 3A by standard electron microscopy methods to be a (322)/vicinal ($\bar{1}$10) pair (N1/N2) and a vicinal (101)/($7\bar{9}\bar{5}$) pair (N3/N4). With these results (figs. S16 to S19), we generated an atomic model (Fig. 3F) of the grain boundary in Fig. 3A.

The faceting of the grain boundary appears to be driven by the formation of a low-energy crystal plane on one of the adjacent grain surfaces, which is a known energy-lowering mechanism (*40*). Bi segregation to the grain boundary is also an energy-lowering mechanism, and these two mechanisms occur such that the net result is Bi segregation to faceted grain boundaries, some of which contain low-index facets. In the case of the grain boundary in Fig. 3, two of the boundary surfaces happen to be of {110} type. Interestingly, these low-index grain surfaces are only vicinal (figs. S18 and S19); the grain boundary plane is not exactly parallel to the beam direction when the crystallite is aligned to a low-index zone axis. In contrast, the high-index surfaces on

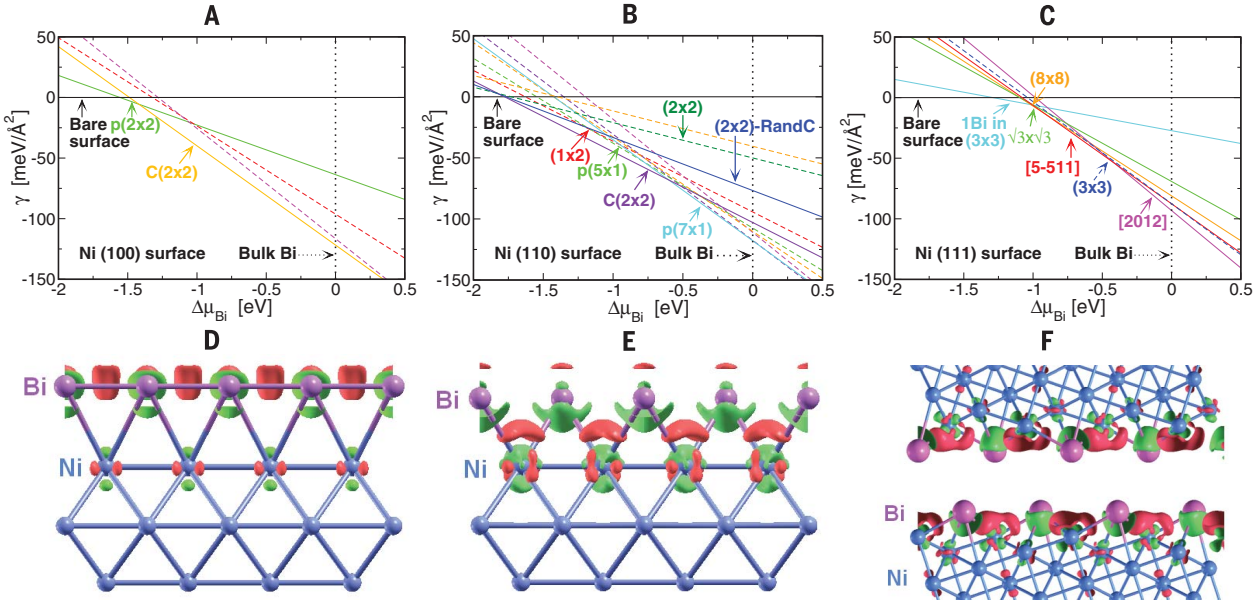

Fig. 2. Results of DFT calculations for Ni-Bi free surfaces and a grain boundary. (**A** to **C**) DFT calculations of surface free energy as a function of chemical potential for various Bi-based superstructures on three different Ni surfaces: (A) Ni(100) surface, (B) Ni(110) surface, and (C) Ni(111) surface. (**D** to **F**) Charge density models based on DFT calculations: (D) unreconstructed [i.e., (1×1)] Bi monolayer on the Ni(100) surface; (E) C(2×2) superstructure on the Ni(100) surface; (F) Σ5-120 grain boundary. In these charge density models, red indicates increased charge density and green indicates charge depletion.

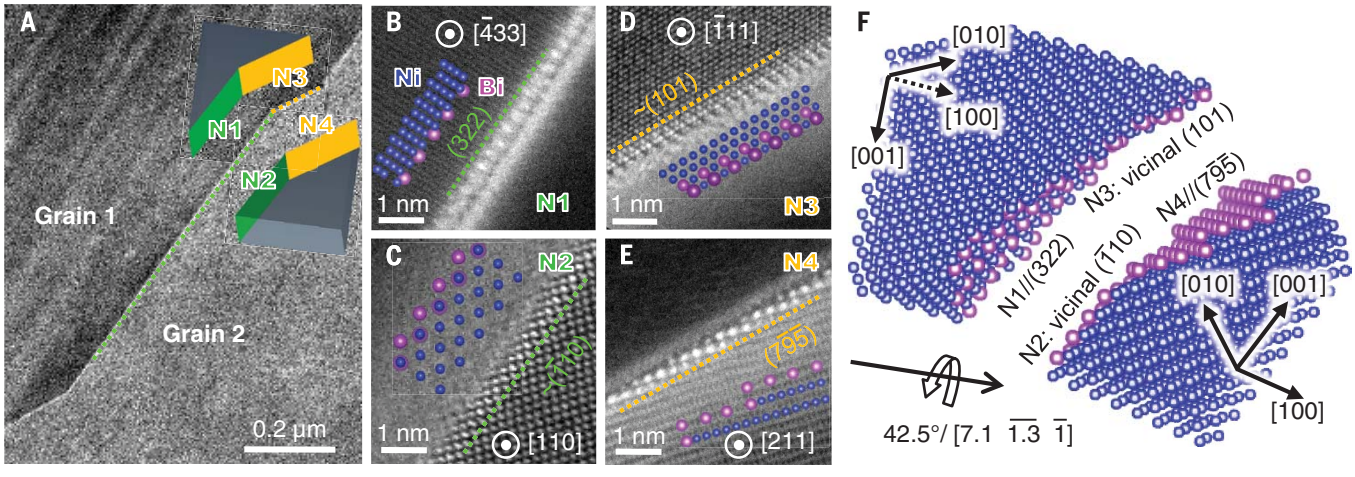

Fig. 3. Grain boundary facets in Bi-doped Ni. (**A**) HAADF-STEM image of a general grain boundary in Bi-doped Ni, which contains micrometer-sized facets. The grain boundary plane pairs ("grain boundary surfaces") of one facet are marked as N1 and N2 (green) and those of a second facet are marked as N3 and N4 (yellow). (**B** to **E**) HAADF-STEM images of the four grain boundary facet planes (with inset atomic diagrams) showing the arrangement of Bi atoms at the grain boundary: (B) N1, (C) N2, (D) N3, (E) N4. (**F**) Schematic model of the atomic structure of these two grain boundary facets. In this model, the grain boundary is intentionally separated by nanometers to show the grain boundary facet surfaces. These HAADF-STEM images were obtained from grain boundary #2 (table S1).

the opposite side of these boundaries are nearly exactly (322) and $(7\bar{9}\bar{5})$, which consist of {111} terraces separated by single-atom-height steps.

The microfacets visible in the general grain boundary can be seen on the intergranular fracture surfaces in scanning electron microscope images (fig. S30). These facets are evidence of the well-known faceting transitions (*41*, *42*) caused by adsorbed impurities at grain boundaries. Atomic-resolution high-angle annular dark field (HAADF)–STEM imaging of the grain boundary facet surfaces present along the 11 general grain boundaries in this study, containing a total of 27 facets (table S1 and figs. S3 to S13), shows that approximately 22% (6 of 27 facets) were terminated by low-index planes and the remaining 78% (21 of 27 facets) were vicinal to low-index planes. Of the 27 facets, we identified superstructures on only 10 facets because of limitations related to STEM imaging and sample geometry. Four such facets were low-index planes and six facets were high-index vicinal planes (table S1 and figs. S24 and S25).

We plotted the crystallographic orientations of the grain boundary facets on a stereographic triangle (Fig. 4A). The stereographic projection is a common graphical method for visualizing crystallographic data (*43*). Here it illustrates that many planes are centered about the 111 and 203 poles of the stereographic projection. Interestingly, the majority of grain boundary surface planes exist along the two edges of the stereographic triangle that run from 001 to 111 and from 001 to 101, demonstrating that these grain boundary surfaces can be produced by pair combinations of these low-index planes (table S2 and fig. S25).

The Bi-Bi atomic spacing in these adsorbate superstructures is large relative to the distances between Ni atoms (Fig. 4B). Because we determined these Bi-Bi distances from STEM images, they could be shorter, as they are projected distances. Nonetheless, our histogram indicates a ~3.25 Å lateral spacing between Bi atoms, which sits between the first (3.07 Å) and the second (3.53 Å) Bi-Bi nearest-neighbor distances in pure Bi metals (*44*). Furthermore, the lateral Bi-Bi distances do not match the Ni-Ni atomic distances [1.74 Å on (100) planes; 2.10 Å on (110) and (111) planes] in pure Ni. The minimization of strain energy from the large atomic size and bonding length mismatch from the pure metals is a reasonable explanation for the formation of the Bi superstructures at the grain boundaries.

Although the primary effect of these Ni-Bi grain boundary superstructures is the embrittlement of the metal, grain boundary superstructures could potentially play a role in electronic, magnetic, and diffusion-related properties as well. It is already known that dopant-based grain boundary complexions can change the electrical resistivity of thick-film resistors (*45*) and the coercivity of Nd-Fe-B magnets (*46*) and could affect the giant spin Hall effect in the Cu-Bi system (*47*). If the complexions in these systems form ordered superstructures, the change of two-dimensional translational symmetry at the grain boundaries would have an impact on related physical properties. Moreover,

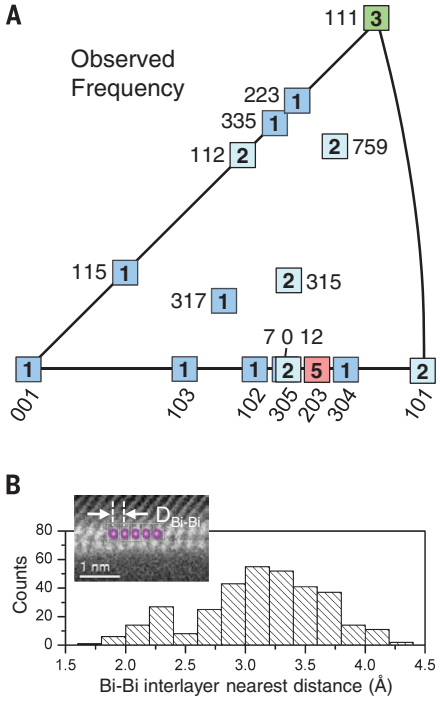

Fig. 4. Grain boundary facet orientations and Bi-Bi distances at grain boundaries in Bi-doped Ni. (**A**) Statistical frequency of grain boundary plane orientations plotted on a stereographic triangle, which includes orientation information for 27 grain boundary facet planes analyzed from 11 general grain boundaries. Numbers of observations of each plane orientation appear within the squares; squares with the same number are colored alike. (**B**) Histogram of the projected in-plane Bi-Bi distances, showing a peak around 3.0 to 3.5 Å, which is between the first and second nearest neighbor Bi-Bi bond length in Bi metal. Inset: A representative STEM image in which the Bi-Bi distance is labeled.

drawing an analogy to the well-known diffusion anisotropy that occurs on reconstructed metal surfaces (*48*), diffusion through superstructures at grain boundaries will likely be anisotropic, and this behavior could potentially be exploited to engineer anisotropic microstructures with enhanced properties.

The discovery of Bi segregation–induced superstructures at general grain boundaries greatly enriches our limited knowledge of the atomic structure of complexions and may offer new insights into a spectrum of structure-related grain boundary properties such as plasticity, diffusivity, and conductivity. We suggest that ordered grain boundary superstructures may indeed be a general, although not necessarily universal, feature of polycrystalline materials. This suggestion is based on an analogy to the reconstruction behavior of free surfaces, in which adsorbates often form periodic structures [e.g., Bi on Cu (*49*)] but can also form disordered overlayers [e.g., S on Cu (*50*)]. Additional studies using TEM and complementary techniques such as APT are needed to determine whether segregation-induced grain boundary superstructures exist in other polycrystalline metals, especially in systems with strong attractive adsorbate-metal pair interactions.

REFERENCES AND NOTES

1. A. P. Sutton, R. W. Baluffi, *Interfaces in Crystalline Materials* (Oxford Univ. Press, 1995).
2. J. P. Buban *et al*., *Science* **311**, 212–215 (2006).
3. M. Yamaguchi, M. Shiga, H. Kaburaki, *Science* **307**, 393–397 (2005).
4. G. Duscher, M. F. Chisholm, U. Alber, M. Rühle, *Nat. Mater.* **3**, 621–626 (2004).
5. S. J. Dillon, M. Tang, W. C. Carter, M. P. Harmer, *Acta Mater.* **55**, 6208–6218 (2007).
6. P. R. Cantwell *et al*., *Acta Mater.* **62**, 1–48 (2014).
7. M. P. Harmer, *Science* **332**, 182–183 (2011).
8. T. Watanabe, *J. Mater. Sci.* **46**, 4095–4115 (2011).
9. M. Tang, W. C. Carter, R. M. Cannon, *Phys. Rev. B* **73**, 024102 (2006).
10. M. Kuzmina, M. Herbig, D. Ponge, S. Sandlöbes, D. Raabe, *Science* **349**, 1080–1083 (2015).
11. J. F. Nie, Y. M. Zhu, J. Z. Liu, X. Y. Fang, *Science* **340**, 957–960 (2013).
12. T. M. Smith *et al*., *Nat. Commun.* **7**, 13434 (2016).
13. T. J. Rupert, *Curr. Opin. Solid State Mater. Sci.* **20**, 257–267 (2016).
14. R. F. Klie, N. D. Browning, *Appl. Phys. Lett.* **77**, 3737–3739 (2000).
15. Z. Yu, Q. Wu, J. M. Rickman, H. M. Chan, M. P. Harmer, *Scr. Mater.* **68**, 703–706 (2013).
16. N. Shibata *et al*., *Nature* **428**, 730–733 (2004).
17. A. Ziegler *et al*., *Science* **306**, 1768–1770 (2004).
18. G. B. Winkelman *et al*., *Appl. Phys. Lett.* **87**, 061911 (2005).
19. U. Alber, H. Müllejans, M. Rühle, *Acta Mater.* **47**, 4047–4060 (1999).
20. A. Kundu, K. M. Asl, J. Luo, M. P. Harmer, *Scr. Mater.* **68**, 146–149 (2013).
21. J. Luo, H. Cheng, K. M. Asl, C. J. Kiely, M. P. Harmer, *Science* **333**, 1730–1733 (2011).
22. L. Yao, S. Ringer, J. Cairney, M. K. Miller, *Scr. Mater.* **69**, 622–625 (2013).
23. M. Herbig *et al*., *Phys. Rev. Lett.* **112**, 126103 (2014).
24. J. Hu, Y. N. Shi, X. Sauvage, G. Sha, K. Lu, *Science* **355**, 1292–1296 (2017).
25. S. Ma *et al*., *Scr. Mater.* **66**, 203–206 (2012).
26. H. Meltzman, D. Mordehai, W. D. Kaplan, *Acta Mater.* **60**, 4359–4369 (2012).
27. A. Morawiec, K. Glowinski, *Acta Mater.* **61**, 5756–5767 (2013).
28. V. Randle, *Mater. Charact.* **47**, 411–416 (2001).
29. L. Priester, *Grain Boundaries: From Theory to Engineering* (Springer, 2012).
30. P. R. Cantwell, S. Ma, S. A. Bojarski, G. S. Rohrer, M. P. Harmer, *Acta Mater.* **106**, 78–86 (2016).
31. R. Gomer, *Rep. Prog. Phys.* **53**, 917–1002 (1990).
32. I. Lyo, E. Kaxiras, P. Avouris, *Phys. Rev. Lett.* **63**, 1261–1264 (1989).
33. See supplementary materials.
34. J. Wang, F. Meng, L. Liu, Z. Jin, *Trans. Nonferrous Met. Soc. China* **21**, 139–145 (2011).
35. K. Glowinski, A. Morawiec, A toolbox for geometric grain boundary characterization. In *Proceedings of the 1st International Conference on 3D Materials Science* (Springer, 2012).
36. E. A. Wood, *J. Appl. Phys.* **35**, 1306–1312 (1964).
37. K. Oura, V. G. Lifshits, A. A. Saranin, A. V. Zotov, M. Katayama, *Surface Science: An Introduction* (Springer, 2003).
38. Q. Gao, M. Widom, *Phys. Rev. B* **90**, 144102 (2014).
39. Q. Gao, M. Widom, *Curr. Opin. Solid State Mater. Sci.* **20**, 240–246 (2016).
40. G. S. Rohrer *et al*., *Z. Metallk.* **95**, 197–214 (2004).
41. M. Menyhard, B. Blum, C. McMahon Jr., *Acta Metall.* **37**, 549–557 (1989).
42. T. Ference, R. Balluffi, *Scr. Metall.* **22**, 1929–1934 (1988).
43. M. De Graef, M. E. McHenry, *Structure of Materials: An Introduction to Crystallography Diffraction and Symmetry* (Cambridge Univ. Press, 2012).
44. P. Cucka, C. Barrett, *Acta Crystallogr.* **15**, 865–872 (1962).

45. Y.-M. Chiang, L. A. Silverman, R. H. French, R. M. Cannon, *J. Am. Ceram. Soc.* **77**, 1143–1152 (1994).
46. O. Gutfleisch *et al.*, *Adv. Mater.* **23**, 821–842 (2011).
47. D. V. Fedorov *et al.*, *Phys. Rev. B* **88**, 085116 (2013).
48. G. Antczak, G. Ehrlich, *Surf. Sci. Rep.* **62**, 39–61 (2007).
49. F. Delamare, G. Rhead, *Surf. Sci.* **35**, 172–184 (1973).
50. G. B. D. Rousseau *et al.*, *Surf. Sci.* **600**, 897–903 (2006).
51. A. I. Kirkland, W. O. Saxton, *J. Microsc.* **206**, 1–6 (2002).

ACKNOWLEDGMENTS

Additional data and images are available in the supplementary materials. We thank W. Zhang (School of Materials Science and Engineering, Tsinghua University) and X. Gu (School of Materials Science and Engineering, University of Science and Technology Beijing) for valuable discussions. Supported by Office of Naval Research Multidisciplinary University Research Initiatives program grant N00014-11-0678 and by U.S. Department of Energy grant DE-SC0014506.

SUPPLEMENTARY MATERIALS

www.sciencemag.org/content/358/6359/97/suppl/DC1
Materials and Methods
Supplementary Text
Figs. S1 to S30
Tables S1 and S2
References (*52–61*)

22 January 2017; accepted 29 August 2017
10.1126/science.aam8256

Segregation-induced ordered superstructures at general grain boundaries in a nickel-bismuth alloy

Zhiyang Yu, Patrick R. Cantwell, Qin Gao, Denise Yin, Yuanyao Zhang, Naixie Zhou, Gregory S. Rohrer, Michael Widom, Jian Luo and Martin P. Harmer

Science **358** (6359), 97-101.
DOI: 10.1126/science.aam8256

Giving grain boundaries more structure

The properties of metals change depending on the composition and structure of grain boundaries in polycrystalline materials. Yu *et al.* discovered a surprising grain boundary superstructure in a nickel-bismuth alloy. Previously, the structure was only known to exist in a specific type of uncommon grain boundary, and experiments had focused on bicrystals. Unexpectedly, this alloy has grain boundary superstructures across a wide range of boundaries in polycrystalline samples. This likely also occurs in other alloys, which opens an avenue for grain boundary engineering to tune the physical properties of metals and ceramics.

Science, this issue p. 97